LARGE EDDY SIMULATION OF MOLTEN STEEL FLOW AND INCLUSION TRANSPORT IN SINGLE PLUG LADLE

Yongbin SHENG[a],Henan SHEN[a],Yanfeng GAO[a],Xin MENG[a],Jixuan WANG[a],Xin YANG[a]*

[a] School of Water Conservancy and Hydropower, Hebei University of Engineering,Handan,056038,China

[*] Corresponding author; E-mail:yangxin@hebeu.edu.cn

Based on a 120-t single plug ladle in a steel plant, a full-scale three-dimensional unsteady steel–slag–gas three phase coupled flow model was established to calculate the multiphase flow field and temperature field inside the ladle during the soft blowing (inclusion removal stage) under different bottom-blowing pressures and initial temperatures. On this basis, the discrete phase model combined with a user defined function was employed to simulate the motion, collision, flotation and removal of inclusions in molten steel. Considering the smoothing effect of the k–ε model and the fact that the driving force acting on inclusions mainly originates from the molten steel, large-eddy simulation was adopted to describe the turbulent flow more accurately and obtain more realistic inclusion motion. The results show that LES captures more detailed flow structures than RANS, leading to a more accurate prediction of inclusion removal efficiency. The inclusion removal rate increases with bottom-blowing argon pressure; at 8 min, the removal rates under 0.2, 0.35 and 0.5 MPa are 70.1%, 74.2% and 76.4%, respectively. Taking 0.35 MPa as an example, the removal rate exceeds 98% within 24 min, and then increases by only to 0.718% between 24 and 30 min. Meanwhile, the initial temperature has a limited effect on inclusion removal efficiency.

Key words: *ladle, inclusion removal, flow field, temperature, large eddy simulation*

1. Introduction

During the secondary refining process, non-metallic inclusions in the ladle can be divided into endogenous inclusions and exogenous inclusions according to their formation methods. Endogenous inclusions directly result from the chemical reactions of inclusion elements and alloy elements during deoxidation and desulfurization in the refining process. Exogenous inclusions mainly come from secondary oxidation, entrainment of protective slag, and erosion of refractory materials [1,2]. The presence of inclusions makes the metal structure non-uniform, resulting in a decrease in the mechanical properties of the metal, such as plasticity, toughness, and fatigue strength. Therefore, effectively removing inclusions is an important task in the secondary refining process. The removal stage of inclusions is mainly concentrated in the later stage of refining. The methods include inclusion removal by standing still, inclusion removal by bottom-blowing argon for soft stirring [3–6] and inclusion removal by electromagnetic stirring [7,8], etc. Among them, the method of removing inclusions by

bottom-blowing argon has been widely used in the removal of inclusions in various types of furnaces due to its advantages such as high safety and easy operation.

However, since the entire refining process is similar to a black box, it is impossible to clearly understand the multiphase flow inside the ladle and the movement and removal laws of inclusions during the soft blowing stage through direct observation or instruments. Only the approximate number of inclusions can be monitored by sampling during the refining process, which poses a huge challenge to process optimization. Therefore, physical simulation and numerical simulation are widely used in research aimed at optimizing inclusion removal. In numerical simulation, Lou *et al* [9] developed a model combining the population balance model (PBM) and computational fluid dynamic (CFD) to calculate the inclusion removal rate. The results show that compared with central injection and eccentric injection, double-plug injection is more conducive to the removal of inclusions. Kown *et al.* [10] established a general inclusion nucleation-growth model to describe the evolution process of inclusions, replacing the step of using experimentally measured inclusions as input conditions for simulation. Hao *et al.* [11] also combined the CFD with the PBM model to study the three-phase flow involving molten steel, slag and argon in an industrial 150 ton ladle, as well as the collision, coalescence and interfacial removal behavior of inclusions. Finally, the relationship between the inclusion removal rate, the bottom blowing flow rate and the different regions was obtained. Duan *et al.* [12] used the discrete phase model (DPM) to study the migration of inclusions with different particle sizes during the ladle standing process. In terms of experiments, Li *et al.* [13,14] used a water model experiments to study the removal rates of inclusions in a two-plug ladle when using slit plugs and porous plugs. They found that porous plugs are beneficial for inclusion removal because they can generate more fine bubbles. In Zheng's experiments [15], emulsion substances were used to replace inclusions, and the effects of time and gas flow rate on the removal of inclusions from the ladle with eccentric bottom blowing through the nozzle and porous plug were studied. Ranjan *et al.* [16] used DPM within CFD to establish a correlation between the inclusion removal rate and the argon gas flow rate. Finally, the results were verified in industrial production, indicating that the prediction error of this model for inclusion evolution and removal is within a reasonable range.

In current studies on ladle inclusion removal, most adopt the PBM model treating inclusions as a continuous phase, while fewer employ a discrete phase approach combined with User Define Function (UDF) to describe inclusion motion and removal. Meanwhile, flow fields are typically calculated using Reynolds Average Navier-Stokes (RANS), which cannot accurately capture the complex inclusion behavior near the slag layer. To develop a more accurate model for practical application, this study takes a single-plug bottom-blown ladle as the prototype and establishes a four-phase fully coupled unsteady steel–slag–gas–inclusion model based on Large Eddy Simulation (LES), which better resolves flow details. All operating and physical parameters are derived from industrial conditions. Numerical simulations provide detailed flow and temperature fields under various conditions. The DPM model is then used to track inclusions, and UDF is applied to simulate their removal process. Finally, the effects of bottom-blowing pressure, initial temperature, and treatment time on inclusion removal rate are quantified, offering theoretical and data support for process optimization.

2. Mathematical model

2.1. Governing equations

(1) A Compressive Interface Capturing Volume of Fluid (VOF) model [17]

The VOF model tracks the interface between continuous phases by solving the continuity equation of the phase volume fraction. The continuity equation for the qth phase can be expressed as

$$\frac{1}{\rho_q}\left[\frac{\partial}{\partial t}\left(\alpha_q\rho_q\right)+\nabla\cdot\left(\alpha_q\rho_q\vec{v}\right)\right]=0 \tag{1}$$

$$\sum_{q=1}^{n}\alpha_q=1 \tag{2}$$

(2) turbulent model

The basic principle of LES is the separation of large-scale and small-scale vortices. The governing equations are obtained by filtering the time-varying N-S equations in the physical space. [18]

The momentum equation is:

$$\frac{\partial}{\partial \mathrm{t}}(\rho\boldsymbol{u}_m)+\nabla\cdot(\rho\boldsymbol{u}_m\boldsymbol{u}_m)= -\nabla P+\nabla\cdot\left[\mu\left(\nabla\boldsymbol{u}_m+\nabla\boldsymbol{u}_m{}^T\right)\right]+\rho\vec{\boldsymbol{g}}+\boldsymbol{F}_{\mathrm{s}}+\boldsymbol{F}_{\mathrm{i}} \tag{3}$$

Filtered momentum equation:

$$\frac{\partial(\rho_{\mathrm{m}}\bar{\boldsymbol{u}}_{\mathrm{m}})}{\partial t}+\nabla(\rho_{\mathrm{m}}\bar{\boldsymbol{u}}_{\mathrm{m}}\bar{\boldsymbol{u}}_{\mathrm{m}})=-\nabla\overline{P}+\nabla[\mu(\nabla\bar{\boldsymbol{u}}_{\mathrm{m}}+\bar{\boldsymbol{u}}_{\mathrm{m}}{}^T)]-\nabla\tau_{ij}+\rho_{\mathrm{m}}\boldsymbol{g}+\boldsymbol{F}_{\mathrm{s}}+\boldsymbol{F}_{\mathrm{i}} \tag{4}$$

τ_{ij} is the subgrid stress:

$$\tau_{ij}=\frac{1}{3}\tau_{kk}\delta_{ij}-2\mu_{\mathrm{t}}\overline{S}_{ij} \tag{5}$$

μ_{t} is the turbulent viscosity:

$$\mu_{\mathrm{t}}=\rho_m L_S^2\left|\overline{S}\right| \tag{6}$$

L_{s} is the mixed length:

$$L_{\mathrm{s}}=\min(\kappa d,\Delta C_{\mathrm{s}}) \tag{7}$$

(3) inclusion transport model

The particle motion equation is obtained from the force balance based on Newton's second law in the lagrangian coordinate system [19]. The expression is as follows:

$$\rho_{\mathrm{i}}\frac{\pi}{6}d_{\mathrm{i}}^3\frac{d\boldsymbol{v}_{\mathrm{i}}}{dt}=\boldsymbol{F}_{\mathrm{d}}+\boldsymbol{F}_{\mathrm{l}}+\boldsymbol{F}_{\mathrm{v}}+\boldsymbol{F}_{\mathrm{p}}+\boldsymbol{F}_{\mathrm{g}}+\boldsymbol{F}_{\mathrm{b}} \tag{8}$$

Where, $\boldsymbol{F}_{\mathrm{d}}$ is the drag force, drag force is also one of the most important forces affecting the particle motion trajectory, and its expression form is:

$$\boldsymbol{F}_{\mathrm{d}}=C_{\mathrm{D}}\frac{3}{4}\frac{\boldsymbol{v}_{\mathrm{m}}}{\rho_{\mathrm{i}}d_{\mathrm{i}}^2}Re_{\mathrm{i}}(\boldsymbol{v}_{\mathrm{m}}-\boldsymbol{v}_{\mathrm{i}}) \tag{9}$$

$\boldsymbol{F}_{\mathrm{l}}$ is the lift force， the expression form is:

$$\boldsymbol{F}_{\mathrm{l}}=C_1\frac{6\mathrm{K}_{\mathrm{s}}u_{\mathrm{eff}}}{\rho_{\mathrm{i}}\pi d_{\mathrm{i}}}\left(\frac{\rho_{\mathrm{m}}\zeta}{u_{\mathrm{eff}}}\right)^{1/2}(\boldsymbol{v}_{\mathrm{m}}-\boldsymbol{v}_{\mathrm{i}}) \tag{10}$$

$\boldsymbol{F}_{\mathrm{p}}$ is the pressure gradient force， the form of expression is:

$$\boldsymbol{F}_{\mathrm{p}} = \frac{\rho_{\mathrm{m}}}{\rho_{\mathrm{i}}} \frac{d\boldsymbol{v}_{\mathrm{m}}}{dt} \tag{11}$$

$\boldsymbol{F}_{\mathrm{v}}$ is the virtual mass force, the form of expression is:

$$\boldsymbol{F}_{\mathrm{v}} = C_{\mathrm{v}} m_i \frac{\rho_m}{\rho_{\mathrm{i}}} (\boldsymbol{v}_{\mathrm{i}} \nabla \boldsymbol{v}_m - \frac{d\boldsymbol{v}_{\mathrm{i}}}{dt}) \tag{12}$$

Since the computational cost of particle collisions is proportional to the square of the number of particles, which consumes a huge amount of computational resources, the concept of parcels is used here. Parcels are a statistical representation of several particles. The O'Rourke algorithm combined with the concept of parcels can estimate the particle collision frequency. Once two particles collide, the algorithm will further determine the collision type. The research by Li *et al.* [20] reported this model in detail.

The actual movement of molten steel is very complex and can be divided into an mean velocity and a pulsating velocity. The main driving force for inclusions is the average velocity of the molten steel, but the pulsating velocity of the molten steel will affects the diffusion of inclusions. Therefore, the random walk model is used to describe the influence of turbulent flow on the movement of inclusion particles.

$$\boldsymbol{u} = \bar{\boldsymbol{u}} + \boldsymbol{u}' \tag{13}$$

$$u' = \xi \sqrt{\overline{u'^2}} \tag{14}$$

Where, $\boldsymbol{u}'$ is the random velocity of molten steel, $\bar{\boldsymbol{u}}$ is the average velocity of molten steel, ξ is a random number with a normal distribution ranging from -1 to 1. For LES, the random velocity fluctuations are equivalent in all directions.

Floating up to the slag layer and being captured by it is the removal method for most inclusions, accounting for more than 90% of the total inclusion removal rate. Other methods such as wall adsorption only account for a very small proportion. Therefore, this paper only discusses the inclusion removal method of capture by the slag layer. In addition, this paper also takes into account the influence of slag layer fluctuations on inclusion removal. The criteria for determining whether inclusions are captured by the slag layer are as follows:

1) During the floating process of inclusions, the velocity towards the slag layer is greater than the critical slip velocity. The expression for the critical slip velocity [21] is:

$$\vec{u_s} = \frac{1}{18} d_p^2 \vec{g} \frac{\rho_l - \rho_p}{\mu_l} \tag{15}$$

2) In the grid where inclusions are judged to be removed, the volume fraction of the slag phase is greater than 0.5.

3) The velocity or velocity component of the inclusions points towards the slag layer.

(4) Solute diffusion equation

On the basis of obtaining a stable flow field, a User Define Scalar (UDS) is used to simulate the motion and diffusion of NaCl solution in the water model in the experiment. The solute diffusion equation of the user-defined scalar is:

$$\frac{\partial \rho \phi}{\partial t} + \nabla \left(\rho \boldsymbol{u} \phi - D \nabla \phi \right) = 0 \tag{16}$$

Where, ϕ is the tracer concentration，D is diffusion constant. On the left side of equation (16), from left to right are the unteady state term, convection term, and diffusion term.

(5) Energy equation

$$\frac{\partial(\rho \mathrm{T})}{\partial t}+\nabla\cdot(\rho \boldsymbol{u} T)=\nabla\cdot\left(\frac{\kappa}{c}\mathrm{grad}T\right)+S_T \tag{17}$$

Where, κ is the thermal conductivity, and c is the specific heat.

2.2. Simulation conditions

The mesh generation of the ladle is shown in Figure 1. All hexahedral structured-elements are used. After mesh independence verification, the total number of meshes is determined to be 1,020,632. Since the slag layer is relatively unstable and the fluctuation range varies, local encryption is carried out on the mesh where the slag layer is located to more accurately capture the steel - slag interface and the slag - gas interface. Secondly, due to the relatively intense movement of the molten steel at the argon inlet and the plume area, local encryption is also carried out on the mesh there. The dimensional parameters of the physical model are shown in Table 1.

Tab. 1. Physical model size

Part	Value
Bottom diameter (mm)	2193
Inclination angle /(°)	3
Plug inner diameter (mm)	102
Inlet eccentricity (mm)	350
Molten steel depth (mm)	1498
Slag layer thickness (mm)	187

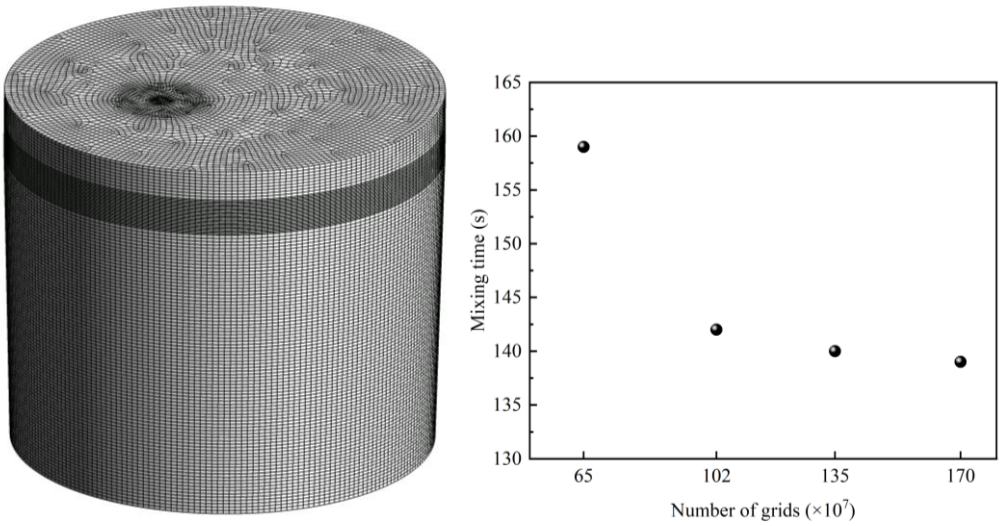

Fig. 1. (a) mesh generation; (b) Grid independence verification

The initial distribution of inclusions should be a random distribution, and the coordinates of these random positions will be obtained through Matlab software. The inclusions are added by means of a file, and all the physical properties, flow rates, and position information of the particles are written into the file. Since the size of the inclusions is at the micrometer level, their impact on the flow of the molten steel is negligible. Meanwhile, since the inclusions move under the influence of the flow field, the removal of the inclusions mainly depends on the flow condition rather than the quantity of the inclusions.

The particle independence verification as shown in fig. 2. Taking into account the computing cost and time, the initial amount of inclusions has been set at 10,000. To be more in line with reality, the particle sizes are divided into 16 types, namely 3, 6, 9, 12, 15, 18, 21, 23, 26, 29, 32, 35, 38, 41, 44, and 47 μm. Every 4 particle sizes are grouped into one group, and there are a total of 4 groups, namely N1, N2, N3, and N4. The inlet is a velocity inlet, and the outlet is above the air layer, which is set as a pressure outlet. Argon enters from the velocity inlet, floats up to the slag layer, pushes open the slag surface, overflows, and then leaves through the pressure outlet. The calculation uses a transient-based pressure solver. The coupling method of pressure and velocity is the SIMPLE algorithm, and the pressure equation selects the pressure staggering option (PRESTO!). The calculation parameters are shown in Table 2. The numerical simulation was carried out using ANSYS FLUENT 19.0, in combination with MATLAB. All data for Figures 6-10 obtained by using functions in the post-processing software cfd-post.

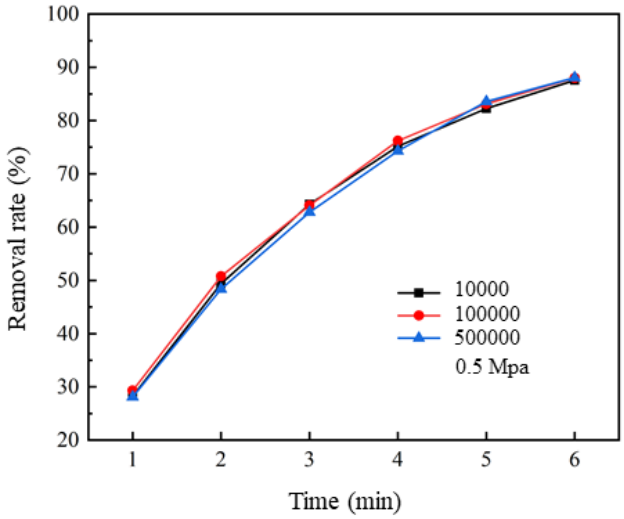

Fig. 2. particle independence verification

Tab. 2. Physical property parameters and boundary condition

Name	Value
Molten steel density(kg/m^3)	8068.5-0.8T
Molten steel viscosity(Pa • s)	0.0246-(1e-05)T
Thermal conductivity of molten steel (W • m^{-1} • K^{-1})	32
Specific heat capacity of molten steel (J • kg^{-1} • K^{-1})	750
Slag density (kg/m^3)	2900
Slag viscosity (Pa • s)	0.0025
Argon density (kg/m^3)	0.85
Gas/steel interfacial tension (N • m)	1.78
Inclusion density (kg/m^3)	3900
Interfacial tension between inclusions and molten steel (N • m)	1.27
Blowing pressure (MPa)	0.2/0.35/0.5

To simplify the calculation of bubble rising and inclusion movement capture, the following assumptions are made:

1) The volume fraction of inclusions is very small and has no effect on the molten steel flow.

2) Ignore chemical reactions and consider bubbles and inclusions as inert spherical particles.

3) The density of the gas remains constant during the rising process.

4) Ignore the aggregation effect between inclusions and only consider the collision effect between inclusions.Model verification

A 1:4 water model experimental platform was established. The ladle model was made of transparent acrylic glass plates. Water was used to replace molten steel, and soybean oil was used to replace the slag layer. Argon gas was used to convert the industrial flow rate to the experimental flow rate through the similarity principle [22–24]. The experimental system is shown in Figure 3(a). First, the argon gas was turned on for blowing. The blowing conditions corresponded to 0.2–0.5 MPa in industrial production. After the flow field and slag eye stabilized, a sodium chloride solution was injected at the slag eye, and the electrical conductivity was recorded. This device currently is placed within Hebei University of Engineering. The experimental period is December 20, 2025, and it was conducted by Yang and Sheng, et al, they are all the authors of this paper. When the conductivity variation was less than 1%, mixing was considered complete and the mixing time was obtained. Each case was repeated five times. The multiphase flow field at the water model scale was then simulated using the same physical properties. A tracer was injected in the same manner and modeled by the UDS, with mixing time evaluated under the same criterion. As shown in Figure 3(b), the experimental and simulated results agree well, demonstrating the accuracy of the model in predicting multiphase flow and solute transport, and thus supporting the reliability of inclusion calculations.

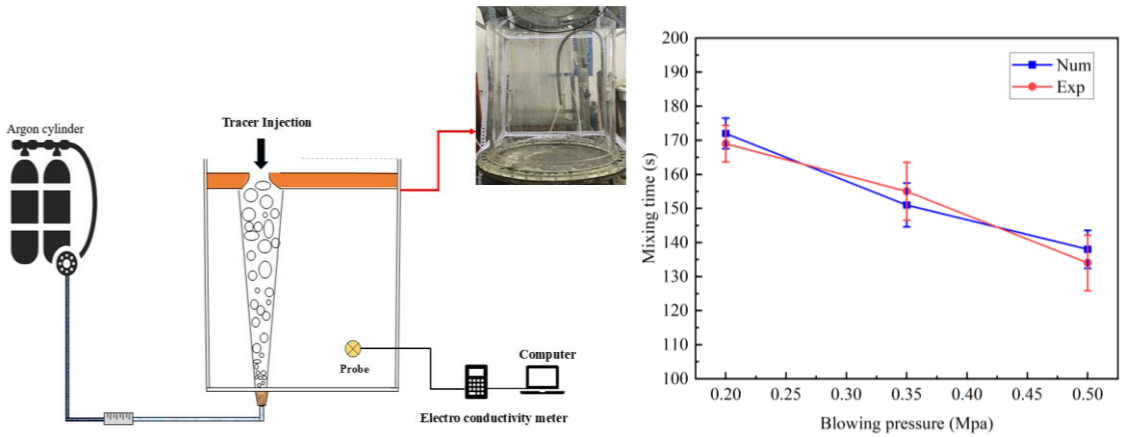

(a) (b)

Fig. 3. Model validation: (a) water model system; (b) mixing time verification

3. Results and discussion

3.1. Flow field and temperature distribution

As shown in Figure 4, after the flow field calculation becomes stable, (a) and (b) use different turbulence models respectively. It can be seen that the flow field calculated by LES has strong randomness. The streamline of molten steel and the fluctuation of the slag layer are closer to reality. There are vortices of various sizes around the rising argon, which indicates that LES has a high precision in controlling vortices. While the flow field obtained by using the Realizable k-ε model based on RANS Reynolds time-averaging shows less randomness, the slag surface fluctuation is smaller, and the smoothing effect is obvious. Since the influence of inclusions on the flow of molten steel can be almost

ignored, the accuracy of the flow field is decisive for the calculation of the movement and removal of inclusions. From the results, it can be predicted that the calculation of inclusions under the LES model will be more accurate.

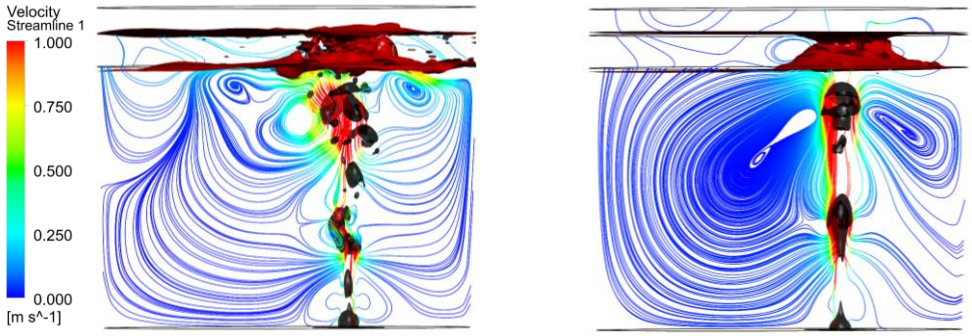

(a) (b)

Fig. 4. Comparison of flow field calculation results: (a) LES; (b) RANS

The internal flow field of the ladle at 0.2 MPa, 0.35 MPa, and 0.5 MPa is calculated as shown in Figure 5. The gas content rate inside the ladle is shown in Figure 6(a). The gas content rate inside the ladle increases with the increase of the bottom blowing pressure. A higher gas content rate can better stir the molten steel to achieve the effects of mixing chemical components and promoting the floating and removal of inclusions. Vortexes appear near the wall below the slag layer. This is formed because the argon gas is resisted by the slag layer. The molten steel flow is not active here. The greater the bottom - blowing pressure, the greater the volume - average velocity, and the flow in the entire ladle cavity is more active, as shown in Figure 6(b).

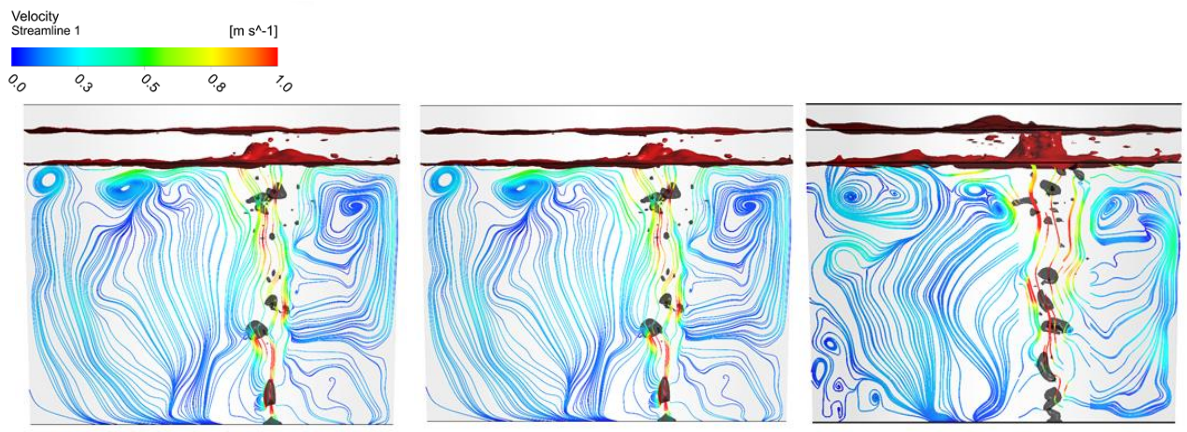

(a) (b) (c)

Fig. 5. Flow field calculation results: (a) 0.2 MPa; (b) 0.35 MPa; (c) 0.5 MPa

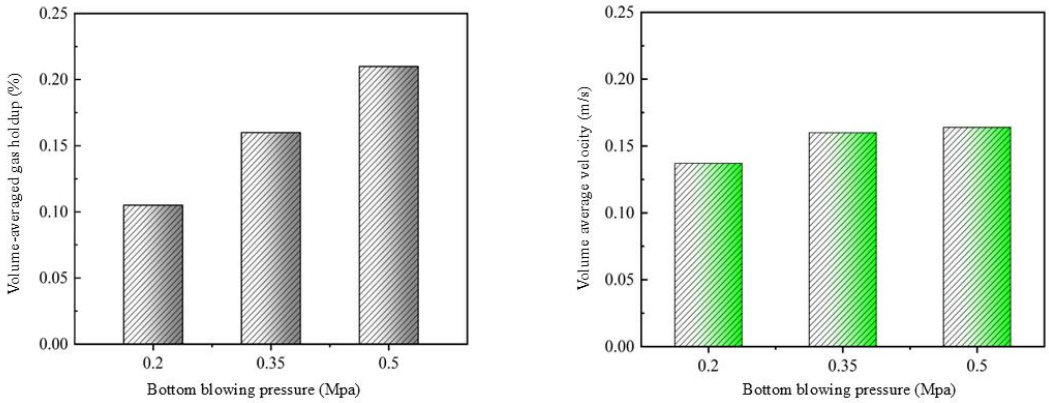

(a) (b)

Fig. 6. Quantification of flow field parameters: (a) volume average gas hold up, (b) volume average velocity

The practical meaning is to provide a prompt for the site. During the refining process, proper insulation measures need to be taken, or before a long period of gentle blowing, the corresponding superheat of the molten steel should be increased to compensate for the temperature drop. Taking the initial temperature of 1800 K as an example, the temperature distribution and temperature drop of the molten steel in the ladle during the soft blowing process are analyzed, as shown in Figure 7. It can be seen that with the continuous soft blowing, the temperature in the ladle gradually decreases and the internal temperature difference gradually increases. Within the calculation time of 8 minutes, the average temperature of the ladle body drops by 9 K, and the maximum temperature difference in the molten steel reaches 13 K.

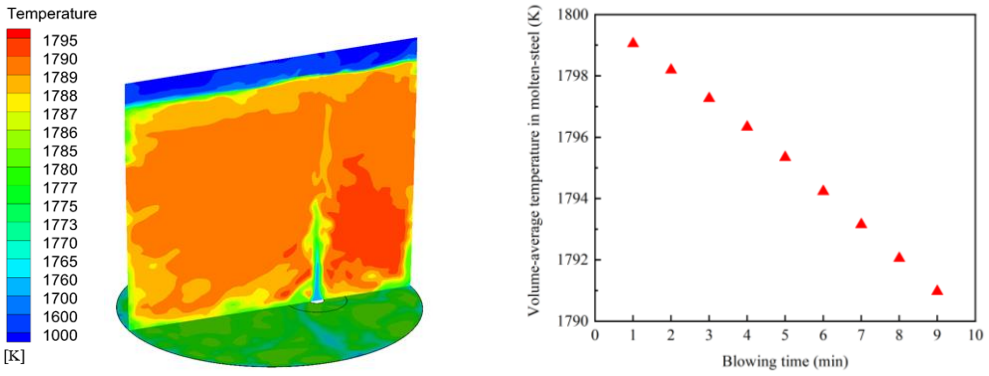

(a) (b)

Fig. 7. The ladle temperature changes with time: (a) Temperature distribution at 480 s; (b) temperature reduction process

3.2. Inclusion movement and removal

As shown in Figure 8, the inclusion removal rate and remaining inclusion quantity within 8 minutes were calculated under bottom-blowing pressures of 0.2, 0.35, and 0.5 MPa. The removal rate increases with pressure, reaching 70.1%, 74.2%, and 76.4%, respectively. The removal process is rapid initially and then slows down, being faster within the first 3 minutes and decreasing significantly after about 6 minutes. When the pressure increases from 0.2 to 0.35 MPa, the removal rate rises by 5.1%, whereas from 0.35 to 0.5 MPa, the increase is only 2.2%, indicating diminishing returns from further pressure increase. Simulation results suggest that 0.35 MPa is close to the critical slag eye opening condition. Beyond this, although inclusions gain higher upward velocity, the enlarged slag eye prevents effective

absorption, causing some inclusions to re-enter the molten steel and limiting further improvement in removal efficiency. As shown in Figures 9, the distribution of remaining inclusions within 8 minutes of bottom blowing time when the bottom blowing conditions are 0.2 MPa, 0.35 MPa and 0.5 MPa.

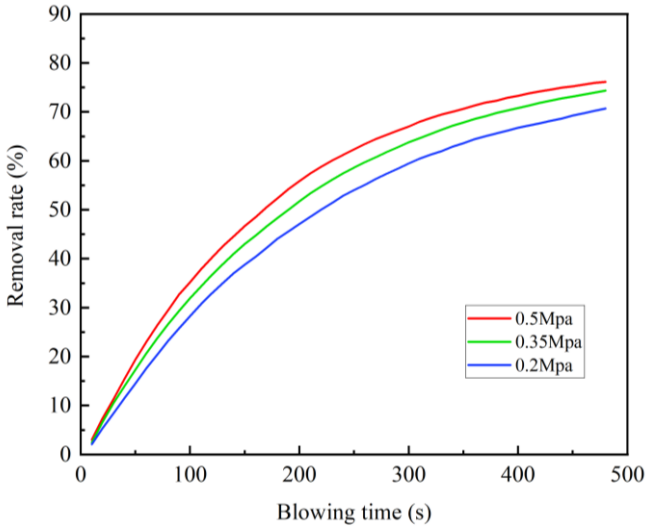

Fig. 8. Inclusion removal rates under different bottom blowing pressures

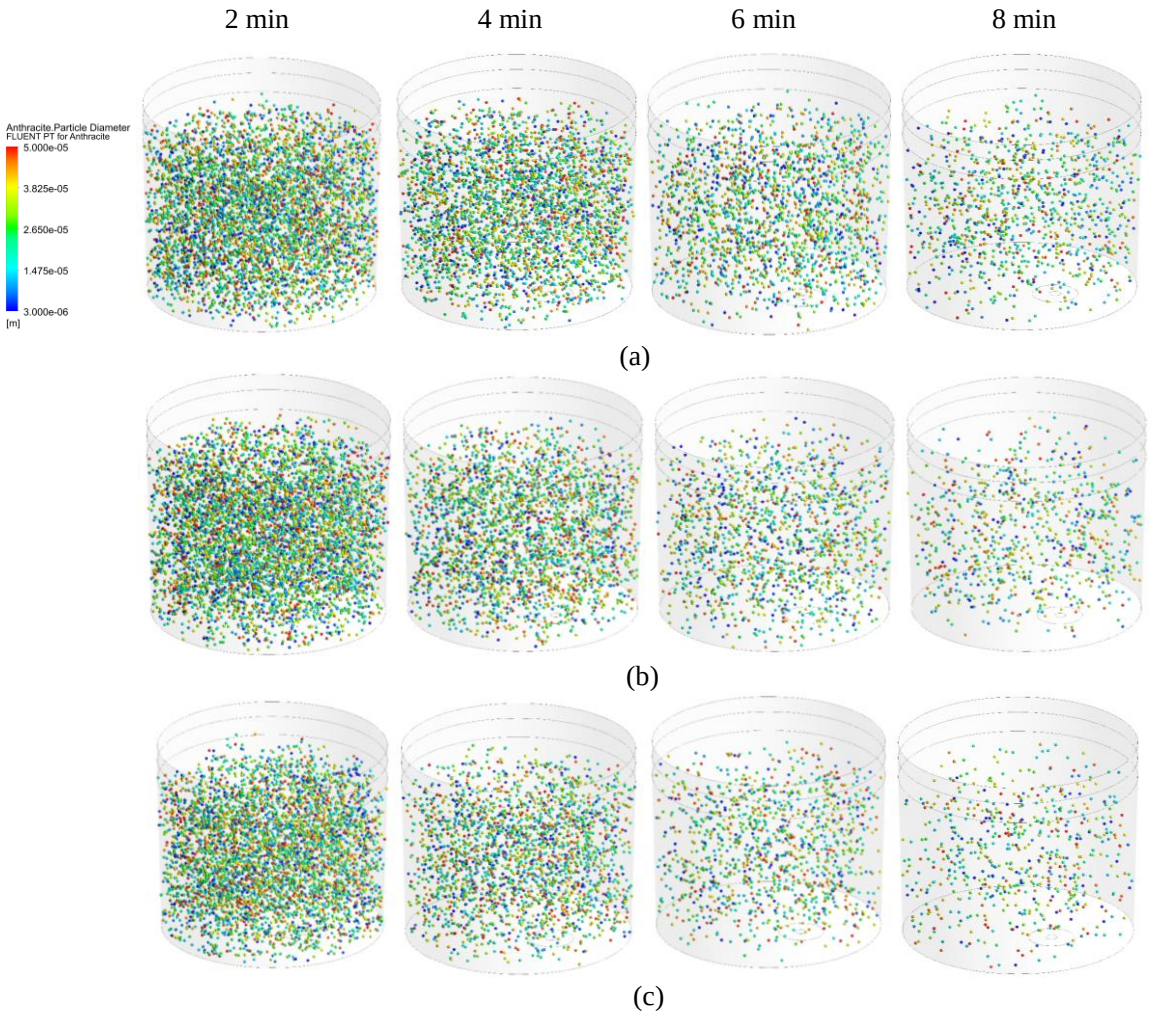

Fig. 9. The number of remaining inclusions: (a) 0.2 MPa; (b) 0.35 MPa; (c) 0.5 MPa

As shown in Figure 10, it shows the removal situation and remaining particles of inclusions in four different particle size groups N1, N2, N3, and N4 over time under three bottom - blowing conditions of 0.2 MPa, 0.35 MPa, and 0.5 MPa. It can be seen that regardless of the flow rate, the removal rate of inclusions with larger particle sizes is greater than that of inclusions with smaller particle sizes. This is because the larger the particle size, the stronger the interaction with the molten steel, and the easier it is to obtain a larger floating velocity. At the same time, the buoyancy it receives is also larger, so it is easier to be removed. The buoyancy received by inclusions with small particle sizes is relatively small, and due to the influence of the turbulent pulsation velocity, a velocity in the direction away from the slag layer may be generated when the removal is determined within the grid, so they cannot be determined to be adsorbed. At the same time, this trend is more obvious during bottom - blowing with a small flow rate, while during bottom - blowing with a large flow rate, such as 0.5 MPa, this trend is no longer obvious.

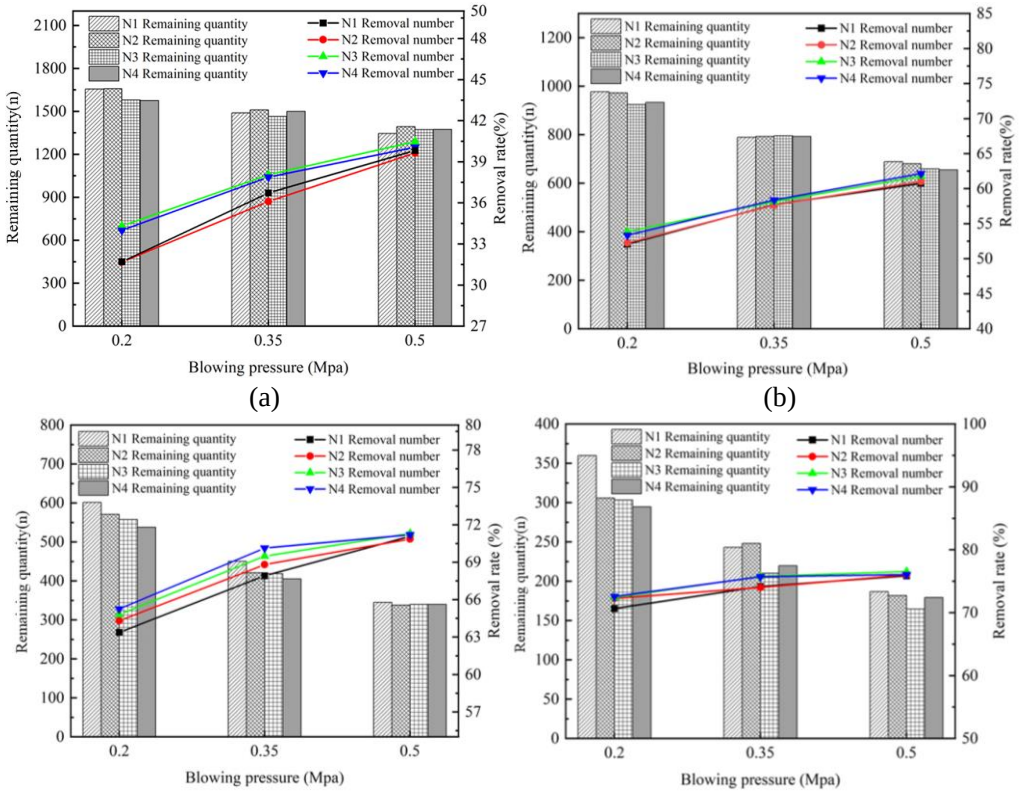

Fig. 10. Removal of inclusions with different particle sizes: (a) 2 min; (b) 4 min; (c) 6 min; (d) 8 min

As shown in Figure 11, inclusion removal rates after 10 minutes are compared for initial molten steel temperatures of 1750 K, 1800 K, and 1850 K. A higher initial temperature leads to a larger temperature difference at the steel–slag interface, slightly enhancing thermophoretic [25] effects on inclusion flotation. Although the removal rate increases marginally with temperature, its overall influence is limited. Based on thermophoretic force and velocity expressions, the thermophoretic velocity is on the order of 10^{-3}, indicating that its primary effect is to increase the randomness of particle motion rather than significantly affect their velocity magnitude.

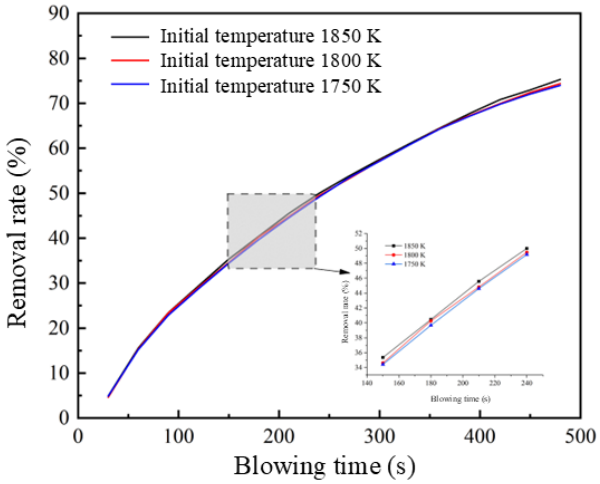

Fig. 11. The relationship between the inclusion removal rate and the initial temperature of molten steel

As shown in Figure 12, the relationship between soft-blowing duration and inclusion removal rate is presented under the optimal condition (bottom-blowing pressure 0.35 MPa and initial temperature 1800 K). The removal rate increases rapidly at first and begins to slow around 11 minutes, becoming nearly unchanged after 24 minutes. Only 0.718% of inclusions are removed between 24 and 30 minutes. In practice, both removal efficiency and temperature drop must be considered. Prolonged treatment increases heat loss, requiring additional energy during reheating to ensure sufficient superheat of the molten steel entering the tundish and mold.

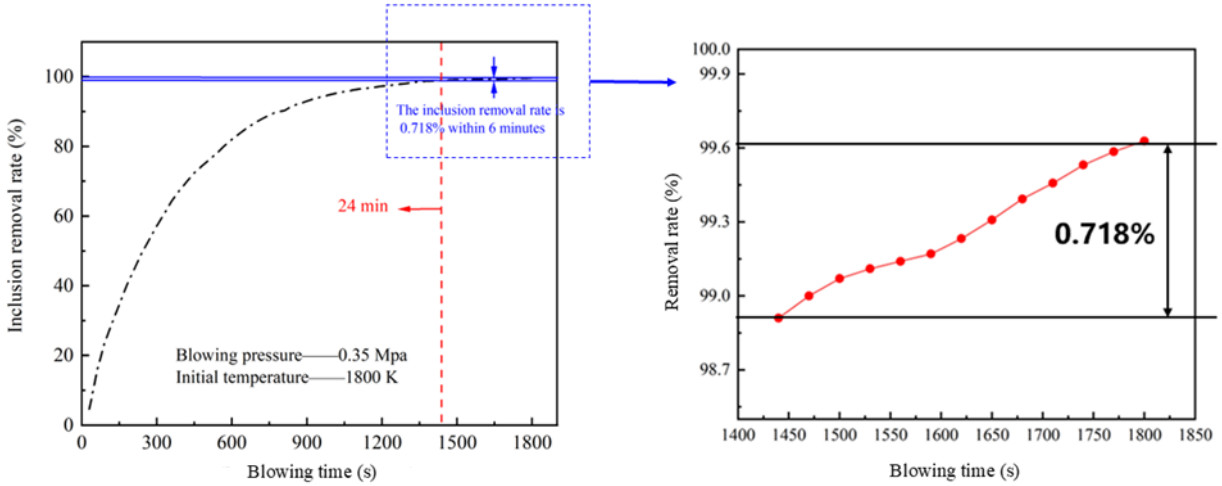

Fig. 12. Full process Inclusion removal rate: (a) the relationship between the inclusion removal rate and time; (b) The removal rate of inclusions changes with time after 24 minutes.

4. Conclusions

In this paper, a three-dimensional unsteady four-phase fully coupled mathematical model of steel-slag-gas-inclusion is established to calculate the multi-physical fields during the refining process of a 120 t ladle in a steel plant. the following conclusions are drawn:

(1) The inclusion removal rate increases with bottom-blowing argon pressure. At 8 min, the removal rates at 0.2, 0.35, and 0.5 MPa are 70.1%, 74.2%, and 76.4%, respectively, while the removal rate begins to slow after 6 min. Larger inclusions are more readily removed due to buoyancy, with the removal rate of the large-size group (N4) being about 5% higher than that of the small-size group (N1).

However, the benefit of increasing pressure diminishes: the removal rate rises by 5.1% from 0.2 to 0.35 MPa, but only by 2.2% from 0.35 to 0.5 MPa.

(2) The calculation time is 8 min. At initial temperatures of 1750, 1800, and 1850 K, the molten steel temperature drops are 7, 9, and 12 K, with maximum temperature differences of 11, 13, and 16 K, respectively. Under the same bottom-blowing pressure, the corresponding inclusion removal rates are 73.87%, 74.36%, and 75.31%, indicating a positive correlation with initial temperature. However, this effect is much weaker than that of bottom-blowing pressure. Therefore, the initial temperature should be determined primarily to compensate for heat loss and maintain sufficient superheat, while increasing it provides limited improvement in inclusion removal.

(3) Taking an inlet pressure of 0.35 MPa as an example, the inclusion removal efficiency increases markedly before 24 min, but shows little improvement thereafter. Between 24 and 30 min, the removal rate is only 0.718% and further decreases beyond 30 min. Although extending the bottom-blowing time enhances inclusion removal, it also leads to significant temperature drop and increased temperature gradients in the molten steel. Therefore, the bottom-blowing time is recommended to be controlled at around 24 min.

(4) This study has established a more accurate mathematical model to simulate the heat transfer, flow and removal of inclusions during the soft blowing process in the steel ladle. The obtained results and trends have certain guiding significance for production practice.

Acknowledgement

This work was supported by the Central Guiding Funds for Local Science and Technology Development (Free Exploration Fundamental Research)： Thermo-economy study and life cycle assessment of solar aided coal-fired unit with carbon capture（246Z4509G）.The authors are grateful for their financial support.

Nomenclature

V	flow rate, L/min
u	the fluid velocity in the x direction, $m \cdot s^{-1}$
v	the fluid velocity in the y direction, $m \cdot s^{-1}$
w	the fluid velocity in the z direction, $m \cdot s^{-1}$
ρ	mass density, $kg \cdot m^{-3}$
t	time, s
μ	dynamic viscosity, $kg \cdot m^{-1} \cdot s^{-1}$
μ_t	turbulent dynamic viscosity, $kg \cdot m^{-1} \cdot s^{-1}$
Ls	dynamic viscosity, $kg \cdot m^{-1} \cdot s^{-1}$
ϕ	tracer concentration
p	pressure, Pa
g	normal terrestrial gravity, $N \cdot kg^{-1}$
T	temperature, K
F_d	drag force, N
F_l	lift force, N
F_P	pressure gradient force, N
F_V	virtual mass force, N
κ	thermal conductivity, $W \cdot m^{-1} \cdot K^{-1}$
u_s	slip velocity, m/s
d	diameter, m
C_D	drag force coefficient, N
C_l	lift force coefficient, N
C_v	virtual mass force coefficient, N
c	specific heat, $J \cdot kg^{-1} \cdot K^{-1}$
D	solutal diffusivity in the liquid, $m^2 \cdot s^{-1}$

Subscript

q	continuous phase
i	each component
l	liquid phase
s	solid phase
p	particle

Superscript

i	each component

References

1] Wang, Q., *et al.*, Numerical Understanding on Refractory Flow-Induced Erosion and Reaction-Induced Corrosion Patterns in Ladle Refining Process, *Metall Mater Trans B, 53* (2022), 3, pp. 1617–1630.

[2] Lou, W., *et al.*, Numerical Simulation of Desulfurization Behavior in Gas-Stirred Systems Based on Computation Fluid Dynamics–Simultaneous Reaction Model (CFD–SRM) Coupled Model, *Metall Mater Trans B, 45* (2014), 5, pp. 1706–1722.

[3] Zhao, J., *et al.*, Numerical simulation on inclusion removal behaviours in refining processes of spring steel, *Ironmaking & Steelmaking, 50* (2023), 5, pp. 430–441.

[4] Zhou, Y., *et al*., Study on the separation process of non-metallic inclusions at the steel−slag interface using water modeling, *Int J Miner Metall Mater, 24* (2017), 6, pp. 627–637.

[5] Zhang, L., *et al*., Inclusion removal by bubble flotation in a continuous casting mold, *Metall Mater Trans B, 37* (2006), 3, pp. 361–379.

[6] Xu, Y., *et al.*, A Numerical Study about the Influence of a Bubble Wake Flow on the Removal of Inclusions, *ISIJ International, 56* (2016), 11, pp. 1982–1988.

[7] Chung, S I., *et al*., Flow Characteristics by Induction and Gas Stirring in ASEA-SKF Ladle, *ISIJ International, 32* (1992), 12, pp. 1287–1296.

[8] Jauhiainen, A., *et al.*, The influence of stirring method on hydrogen removal during ladle treatment, *Steel Research, 73* (2002), 3, pp. 82–90.

[9] Lou, W., *et al.*, Numerical Simulations of Inclusion Behavior and Mixing Phenomena in Gas-stirred Ladles with Different Arrangement of Tuyeres, *ISIJ Int, 54* (2014), 1, pp. 9–18.

[10] Kwon, Y J., *et al.*, A CFD-based Nucleation-growth-removal Model for Inclusion Behavior in a Gas-agitated Ladle during Molten Steel Deoxidation, *ISIJ Int, 48* (2008), 7, pp. 891–900.

[11] Hao, Y., *et al.*, Study on Collision–Coalescence and Removal Behavior of Inclusions in Liquid Steel Under Gas Stirring in Ladle Refining, *Metall Mater Trans B, 56* (2025), 6, pp. 6877–6891.

[12] Duan, H., *et al.*, Fluid Flow, Thermal Stratification, and Inclusion Motion During Holding Period in Steel Ladles, *Metall Mater Trans B, 50* (2019), 3, pp. 1476–1489.

[13] Li, X., *et al.*, Investigation on the Alloy Mixing and Inclusion Removement through Using a New Slot-Porous Matched Tuyeres, *Metals, 13* (2023), 4, pp. 667.

[14] Li, X., *et al.*, Inclusion Removements in a Bottom-Stirring Ladle with Novel Slot-Porous Matched Dual Plugs, *Metals, 12* (2022), 1, pp. 162.

[15] Zheng, S., Zhu, M., Water model study on removing inclusions in a ladle with argon injected through nozzle and porous plug(In Chinese), *Acta metallurgica sinica, 42* (2006), 11, pp. 1143 1148.

[16] Ranjan, M., *et al.*, Validated kinetic modelling of ladle furnace process for predicting inclusions in API steel grade, *Ironmaking & Steelmaking: Processes, Products and Applications*, (2024), https://doi.org/10.1177/03019233241292379.

[17] Hirt, C W., Nichols, B D., Volume of Fluid (VOF) Method for the Dynamics of Free Boundaries, *Journal of Computational Physics, 39* (1981), 1, pp. 201–225.

[18] Meneveau, C., *et al.*, A Lagrangian Dynamic Subgrid-Scale Model of Turbulence. *Journal of Fluid Mechanics, 319* (1996), pp. 353–385.

[19] Jain, D., *et al.*, Numerical Study of Coalescence and Breakup in a Bubble Column Using a Hybrid Volume of Fluid and Discrete Bubble Model Approach, *Chemical Engineering Science, 119* (2014), pp. 134–146.

[20] Li, L., *et al.*, Modeling of Gas-Steel-Slag Three-Phase Flow in Ladle Metallurgy: Part II. Multi-scale Mathematical Model, *ISIJ International, 57* (2017), 11, pp. 1980–1989.

[21] Rückert, A., *et al*., Particle Distribution and Separation in Continuous Casting Tundish, *Steel Research International, 80* (2009), 8, pp. 568–574.

[22] Tang, H., *et al*., A novel dual plugs gas blowing mode for efficient ladle metallurgy, *Ironmaking & Steelmaking, 46* (2019), 5, pp. 405–415.

[23] Li, L., *et al.*, Effect of Salt Solution Tracer Dosage on the Transport and Mixing of Tracer in a Water Model of Asymmetrical Gas-Stirred Ladle with a Moderate Gas Flowrate, *Symmetry, 16* (2024), 5, pp. 619.
[24] Chen, C., *et al.*, Effect of Salt Tracer Amount on the Mixing Time Measurement in a Hydrodynamic Model of Gas-Stirred Ladle System, *Steel research int., 84* (2013), 9, pp. 900–907.
, *Internation journal of heat and mass transfer,*

Submitted: 19.04.2026.
Revised: 21.08.2026.
Accepted: 27.08.2026.